Linking in-situ charge accumulation to electronic structure in doped SrTiO₃ reveals design principles for hydrogen evolving photocatalysts.

Benjamin Moss[1,2], Qian Wang[3,4], Keith T. Butler[5], Ricardo Grau-Crespo[6] Shababa Selim[1,2], Anna Regoutz[7], Takashi Hisatomi[8], Robert Godin[1,9], David J. Payne[10], Andreas Kafizas[1,11], Kazunari Domen[6,12], Ludmilla Steier[1*] and James R. Durrant[1,2]

Abstract

Recently, record solar to hydrogen efficiencies have been demonstrated using La,Rh co-doped SrTiO₃ (La,Rh:SrTiO₃) incorporated into a low cost and scalable Z-scheme device, known as a photocatalyst sheet. However, the unique properties that enable La,Rh:SrTiO₃ to support this impressive performance are not fully understood. Combining in-situ spectroelectrochemical measurements with density functional theory and photoelectron spectroscopy produces a depletion model of Rh:SrTiO₃ and La,Rh:SrTiO₃ photocatalyst sheets. This reveals remarkable properties, such as deep flatband potentials (+2 V_RHE) and a Rh oxidation state dependent reorganisation of the electronic structure, involving the loss of a vacant Rh 4d mid gap state. This reorganisation enables Rh:SrTiO₃ to be reduced by co-doping without compromising p-type character. In-situ time resolved spectroscopies show the electronic structure reorganisation induced by Rh reduction controls electron lifetime in photocatalyst sheets. In Rh:SrTiO₃, enhanced lifetimes can only be obtained at negative applied potentials, where the complete Z-scheme operates inefficiently. La co-doping fixes Rh in the 3+ state, resulting in long-lived photogenerated electrons even at very positive potentials (+1 V_RHE), where both components of the complete device operate effectively. This understanding of role of co-dopants provides new insight into the design principles for water splitting devices based on bandgap engineered metal oxides.

Wide band gap binary and ternary metal oxides such as TiO₂,[1] SrTiO₃,[2] are often considered benchmark photocatalysts due to their chemical stability, low-cost and high quantum yields (>70% for unassisted water splitting).[3,4] However, their large optical band gap limits solar harvesting to the UV and solar-to-hydrogen (STH) conversion efficiency to ~2%.[5] One potential strategy to introduce visible light absorption is to modify the band structure of wide band gap oxides. For example, visible light harvesting in TiO₂ has been achieved through doping with carbon[6], nitrogen[7] or transition metals.[8,9] Improvements have been chequered,

[1] Department of Chemistry, Imperial College London, London, W12 0BZ, UK

[2] Centre for Plastic Electronics, Imperial College London, Prince Consort Road, London SW7 2BZ, UK

[3] Department of Chemical System Engineering, School of Engineering, The University of Tokyo, 7-3-1 Hongo, Bunkyo-ku, Tokyo 113-8656, Japan

[4] Department of Chemistry, University of Cambridge, Lensfield Road, Cambridge CB2 1EW, UK

[5] SciML, Scientific Computing Division, Rutherford Appleton Laboratory, Harwell, OX11 0QX, UK

[6] Department of Chemistry, University of Reading, Whiteknights, Reading, RG6 6AD, UK

[7] Department of Chemistry , University College London, 20 Gordon Street, London, WC1H 0AJ, UK

[8] Research Initiative for Supra-Materials, Interdisciplinary Cluster for Cutting Edge Research, Shinshu University, 4-17-1 Wakasato, Nagano-shi, Nagano 380-8553, Japan

[9] Department of Chemistry, University of British Columbia, Kelowna, BC, V1V 1V7, Canada

[10] Department of Materials, Imperial College London, London, SW7 2AZ, UK

[11] Grantham Institute, Imperial College London, London, SW7 4AZ, UK

[12] Office of University Professor, The University of Tokyo, 7-3-1 Hongo, Bunkyo-ku, Tokyo 113-8656, Japan

* correspondence to: l.steier@imperial.ac.uk

uncovering significant challenges in translating enhanced visible light harvesting into improved STH efficiency.[1,10] With notable exceptions,[6,7] marginal gains or even losses in overall photon conversion efficiency are generally observed in most studies, despite improved light absorption.[9,11,12] The reasons for these losses are often unclear, but are broadly attributed to the inadvertent formation of localised dopant states, associated with short carrier diffusion lengths and low conductivities, and/or charge compensating defect levels, which may act as recombination centres.[13,14] As such, doping for visible light activity has often been suggested to be a less promising strategy for producing efficient photocatalysts in comparison to other methods.[14,15–22]

Recently Domen and co-workers have demonstrated a band gap engineered wide band gap oxide (La,Rh co-doped $SrTiO_3$) exhibiting QYs in the visible of 33% and overall STH efficiencies exceeding 1% using a 'photocatalyst sheet' device architecture.[23–26] This represents a record for a Z-scheme water splitting device. Sheets are constructed by embedding a layer of n-type $Mo:BiVO_4$ and p-type $La,Rh:SrTiO_3$ semiconducting particles into a solid conductive mediator such as gold or carbon. Pioneering ex-situ studies of $Rh:SrTiO_3$[27–31] powders have indicated that Rh^{4+} substitution at Ti^{4+} sites introduces filled Rh states above the $SrTiO_3$ valence band (VB) as well as a vacant mid gap state.[27] Reduction of Rh^{4+} to Rh^{3+} by chemical reduction or co-doping supresses this state.[27,29] Electron trapping in $Rh:SrTiO_3$ has been previously observed in ex-situ transient absorption experiments on nanosecond timescales and was attributed to trapping in the vacant mid gap state, thus explaining the low efficiency of Rh^{4+} doped systems.[11–14] However, the absence of a semiconductor electrolyte interface in these studies means that the intrinsic capacity of $Rh:SrTiO_3$ and related materials to separate charge remains unexplored. Further, key operational parameters such as the potential drop when contacted with electrolyte remain unmeasured, limiting understanding of the factors that may facilitate charge separation in this remarkable material.[27,29] Herein, we combine time resolved optical spectroscopies performed in situ on $(La),Rh:SrTiO_3$ photocatalyst sheets with direct electronic structure measurements supported by density functional theory (DFT) to reveal the remarkable interplay between Fermi level position, Rh 4d structure and band bending/charge separation in $Rh:SrTiO_3$ materials.

Figures 1a-b show optical absorption spectra and photographs of $SrTiO_3$, $Rh:SrTiO_3$, hydrogen reduced $Rh:SrTiO_3$ ($H_2-Rh:SrTiO_3$) and $La,Rh:SrTiO_3$ powders used to fabricate photocatalyst sheets. XRD showed all powders to be phase pure – consisting of single perovskite phase (Supplementary Fig. S0). Upon doping $SrTiO_3$ with Rh, a purple powder is obtained showing a 0.4 eV red-shift in the effective optical band gap (Tauc plots in Supplementary Fig. S1) alongside two strongly broadened sub-bandgap absorption features between ~500-800 nm and ~900-1200 nm. After chemically reducing $Rh:SrTiO_3$ in a hydrogen atmosphere, the powder turns bright yellow and the absorption spectrum shows a further red-shift in the effective band edge and the disappearance of the additional absorption features, consistent with previous observations.[8,27] XPS indicates the reduction of Rh^{4+}, predominantly to Rh^{3+} (Supplementary Fig. S2.1-S2.3). A similar effect is observed when $Rh:SrTiO_3$ is co-doped with La. Here, a light-yellow powder is obtained. XPS reveals a Rh:La ratio of 1:1 in our samples and the reduction of Rh^{4+} to Rh^{3+}. This is in agreement with previous studies which reported that La^{3+} substitution at Sr^{2+} sites can effectively facilitate the reduction of Rh^{4+} to Rh^{3+} via an ionic charge compensation mechanism,[23,29,30] and shows that La co-doping has an effect analogous to chemical reduction.
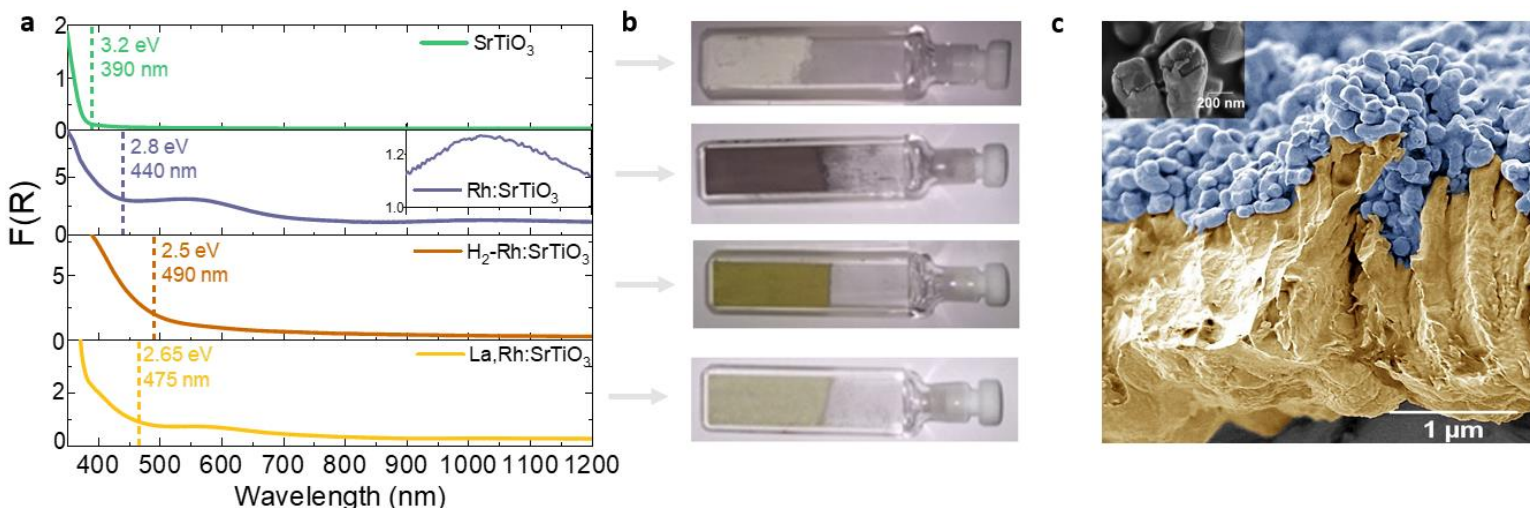
Figure 1. The colour of doped and undoped SrTiO₃ powders and the morphology of photocatalyst sheets. (a) Optical absorption spectra, plotted in dimensionless units of the Kubelka-Munk function, F(R), for SrTiO₃, Rh doped SrTiO₃ (Rh:SrTiO₃), hydrogen reduced Rh:SrTiO₃ (H₂-Rh:SrTiO₃) and La,Rh co-doped SrTiO₃ (La,Rh:SrTiO₃). Dotted lines show the fitted effective optical band gap extracted from Supplementary Fig. S1. (b) Photographs of the powders to indicate the color of the aforementioned materials. (c) A typical cross-sectional SEM image of the photocatalyst sheets studied herein, showing a monolayer of partially sintered (La),Rh:SrTiO₃ particles (blue) embedded (see inset) in a 2 μm thick gold back contact (yellow). This is colored according to EDX mapping results (Supplementary Fig. S3).

We fabricated photocatalyst sheet half-electrodes from these powders using a modified particle transfer method (see Methods). Cross-sectional scanning electron microscopy (SEM) images (Fig. 1c, EDX mapping in Supplementary Fig. S3) show that these modified photocatalyst sheets consist of a layer of partially sintered oxide particles embedded in a 2 μm thick Au back contact. These photocatalyst sheet half-electrodes permit us to study the properties of Rh:SrTiO₃ and La,Rh:SrTiO₃ under operational conditions, meaning in electrolyte solution, under illumination and in the potential window a z-scheme device is likely to operate during water splitting. As such the results shown in Figure 2 track electrode processes and transformation in situ and thus differ from ex situ studies published thus far. Spectroelectrochemical (SEC) measurements of a Rh:SrTiO₃ photocatalyst sheet shown in Figure 2a track the change in optical absorption at the surface of Rh:SrTiO₃ as the potential is varied from 1.1 V$_{RHE}$ towards -0.2 V_{RHE}. The differential absorption spectra at more negative potentials show a redshift in absorption around the effective band edge (positive ΔF(R)) that occurs in concert with the loss of absorption from the sub-band gap features (negative ΔF(R)). This trend is reversible when the potential is scanned in the opposite direction (Supplementary Fig. S4a). ΔF(R) of the sub-band gap features exhibits sigmoidal behaviour with respect to applied potential, typical of a redox couple, with E$_{1/2}$ located at 0.52 V$_{RHE}$ (Supplementary Fig. S4b and Fig. 2f discussed further below). A similar differential absorption spectrum can be obtained by subtracting the absorption spectrum of (Rh⁴⁺) Rh:SrTiO₃ from (Rh³⁺) H₂-Rh:SrTiO₃ (Fig. 2b). We therefore attribute the optical changes observed in Rh:SrTiO₃ photocatalyst sheets under applied potential to the reversible reduction of Rh⁴⁺ to Rh³⁺ within the space charge layer. This is corroborated by cyclic voltammograms showing a reversible redox wave within the same potential window (Supplementary Fig. S4c). In contrast, the optical absorption of La,Rh:SrTiO₃ sheets shows negligible absorption changes over this potential range (Supplementary Fig. S4d), consistent with an ionic charge compensation mechanism, which fixes Rh predominantly in the 3+ oxidation state independent of applied bias.
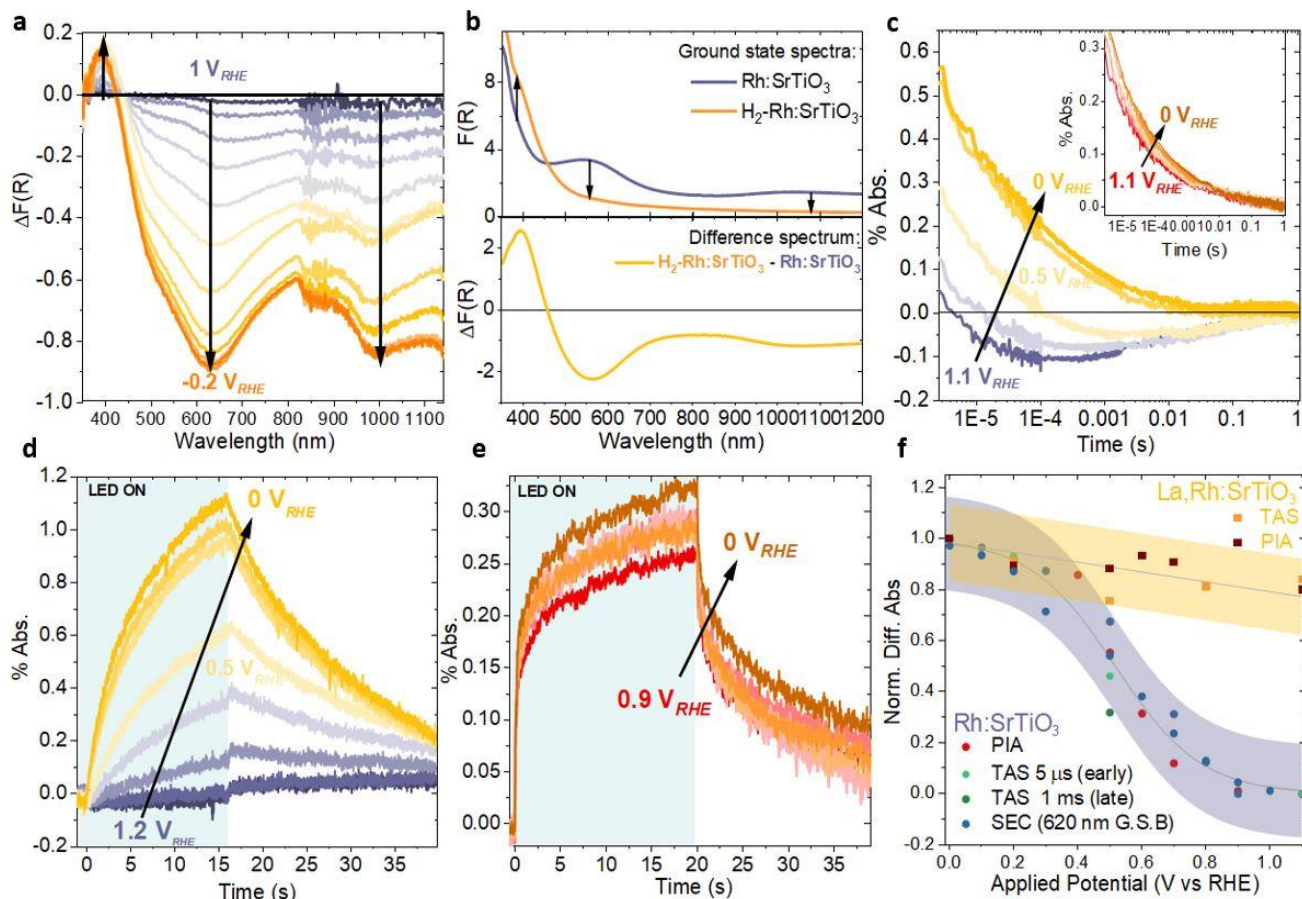
Figure 2. Connecting the Rh oxidation state to charge carrier dynamics of (La,)Rh:SrTiO₃ photocatalyst sheets. (a) Spectroelectrochemical (SEC) difference spectra of Rh:SrTiO₃ photocatalyst sheets, showing the change in optical absorption upon applying negative potentials in comparison to a reference spectrum taken at 1.1 V_{RHE} [ΔF(R) = F(R($V_{applied}$))-F(R(1.1 V_{RHE}))]] (b) The absorption spectra of Rh:SrTiO₃ and H₂-Rh:SrTiO₃ (top) can be subtracted to produce a difference spectrum [ΔF(R) = F(R(H₂-Rh:SrTiO₃))-F(R(Rh:SrTiO₃))]] (bottom) similar to that seen in (a). (c) Transient absorption kinetics of electrons in Rh:SrTiO₃ and La,Rh:SrTiO₃ (inset) photocatalyst sheets measured over a range of applied potentials (1.1, 0.8, 0.5, 0.3 and 0 V_{RHE}). Samples were excited with a 355 nm laser pulse (7 ns, 400 $\mu J/cm^2$) with a 1250 nm probe light used to monitor electrons. (d) Photoinduced absorption (PIA) kinetics in Rh:SrTiO₃ and (e) La,Rh:SrTiO₃ photocatalyst sheets at various applied potentials, tracking conduction band electrons monitored at 1250 nm. The sample was irradiated with 365 nm LED light for several seconds (8 mW cm⁻², shaded region) before the LED was switched off again. (f) Overlay of normalised differential absorption as a function of potential extracted from: i) the 620 nm bleaching signal in SEC, normalised against the bleaching minimum at 620 nm and 0 V_{RHE} (Fig. 2a) ii) TA signals measured at 5 µs and 1 ms normalised against the 0 V_{RHE} signal at these times (Fig. 2c) and iii) the maximum PIA amplitude, normalised using the PIA maximum at 0 V_{RHE} (Fig. 2d,e) for Rh:SrTiO₃ and La,Rh:SrTiO₃ photocatalyst sheets. All data points for Rh:SrTiO₃ sheets were then fitted to a sigmoidal (logistic decay type) function, yielding a midpoint at 0.52 V_{RHE}. A linear function was used to fit datapoints for La,Rh:SrTiO₃ sheets. Electrolyte in all measurements: 0.1 M Na₂SO₄ solution (pH 7).

Figure 2c shows potential dependent transient absorption (TA) of (La),Rh:SrTiO₃ photocatalyst sheet half-electrodes. We excited samples with a UV laser flash and monitored the kinetics at 1250 nm, spanning the µs-s timescales relevant to water splitting reactions[32]. TA studies of SrTiO₃ and La,Rh:SrTiO₃ using electron and hole scavengers (Supplementary Fig. S5.1-5.2) indicate that 1250 nm probes the absorption of photogenerated electrons relatively close in energy to the conduction band (hereafter 'CB electrons', though we note that in oxide materials these CB electrons are not necessarily of the same nature as early timescale (i.e. ps-ns) free electrons in the CB). In La,Rh:SrTiO₃ sheets (inset Fig. 2c), a positive 1250 nm transient absorption is observed, showing power law decay kinetics invariant over the range of potentials studied (TA analysis in Supplementary Fig. 5.3a). Only a modest initial amplitude dependence on applied potential (<10%) is found. In the case of Rh:SrTiO₃ photocatalyst sheets, the TA kinetics show two distinct decay regimes governed by applied potential. At positive potentials (e.g. 1.1 V_{RHE}) a transient bleach (loss of absorption) is observed on the µs-

4

ms timescale. SEC of Rh:SrTiO$_3$ sheets (Fig. 2a) indicates that a loss of sub-band gap absorption is associated with the removal of Rh^{4+} states from the system. Consequently, we attribute the 1250 nm bleach observed in Rh:SrTiO$_3$ sheets at positive applied potentials to a loss of Rh^{4+} states after excitation, presumably related to electron trapping by Rh^{4+} states. This is in agreement with *ex-situ* observations made by Murthy *et al*[33] and is also concordant with a linear dependence of the amplitude of this feature on laser intensity (Supplementary Fig. 5.3b,c). In contrast, at potentials close to 0 V_{RHE}, positive transients are observed with power law decay kinetics *identical* to La,Rh:SrTiO$_3$ (Supplementary Fig. S5.3d). By extension, we therefore also assign absorption at 1250 nm in Rh:SrTiO$_3$ sheets at negative applied potentials to CB electrons. A change in the fate of photogenerated electrons in Rh:SrTiO$_3$ photocatalyst sheets is further supported by the TA spectrum of Rh:SrTiO$_3$ (Supplementary Fig. S5.4a), which is similar to La,Rh:SrTiO$_3$ at negative potentials but dissimilar at positive potentials (Supplementary Fig. S5.4b).

To evaluate photocatalyst sheets under operational conditions and study the accumulation of charges at the oxide surface available for catalysis, we monitored electron dynamics (1250 nm probe) during and after long pulse illumination (15-20s) with a 365 nm LED (Fig. 2d-e and Methods). The resulting photoinduced absorption (PIA) spectra of Rh:SrTiO$_3$ and La,Rh:SrTiO$_3$ sheets (Supplementary Fig. S5.5a-c) exhibit a similar shape and potential dependence to the respective TA spectra (Supplementary Fig. 5.4a,b), indicating that the same species are monitored at 1250 nm in both experiments. We observe that electron accumulation during irradiation is strongly potential-dependent in Rh:SrTiO$_3$ photocatalyst sheets (Fig. 2d), but broadly potential-independent in La,Rh:SrTiO$_3$ sheets (Fig. 2e). At positive potentials (e.g. 1.1 V_{RHE}) Rh:SrTiO$_3$ shows a small ground state bleach. This signal transforms into a growing positive absorption as the applied potential approaches 0 V_{RHE}. After the LED is turned off, the small bleach signal at positive applied potentials recovers on a similar timescale (~100 ms) to that seen in TAS (Fig. 2c). In contrast, at negative potentials, absorption signals persist for tens of seconds after the LED is turned off.

Figure 2f summarises the potential dependence of our in-situ studies; plotting signal amplitudes of SEC (Fig. 2a), TA (Fig 2c) and PIA (Fig. 2d,e) against electrode potential for Rh:SrTiO$_3$ and La,Rh:SrTiO$_3$ photocatalyst sheets. In Rh:SrTiO$_3$ photocatalyst sheets, normalised TA signals, as well as the maximum PIA amplitude of accumulated electrons track the redox wave behaviour of our SEC measurements (Supplementary Fig. S4b). This overlay clearly shows that the photogeneration of long-lived conduction band electrons is strongly linked to Rh^{4+} reduction in Rh:SrTiO$_3$ sheets. In summary, this data indicates that under operational conditions, Rh:SrTiO$_3$ photocatalyst sheets only generate long-lived electrons for biases << 0.52 V_{RHE} (i.e. $E^{Rh4+/Rh3+}$), whilst La,Rh:SrTiO$_3$ sheets produce long-lived electrons even under strongly positive (+1 V_{RHE}) potentials. As we later discuss, the ability to accumulate charge at positive potentials is critical to the efficient operation of the complete water splitting Z-scheme in photocatalyst sheets.
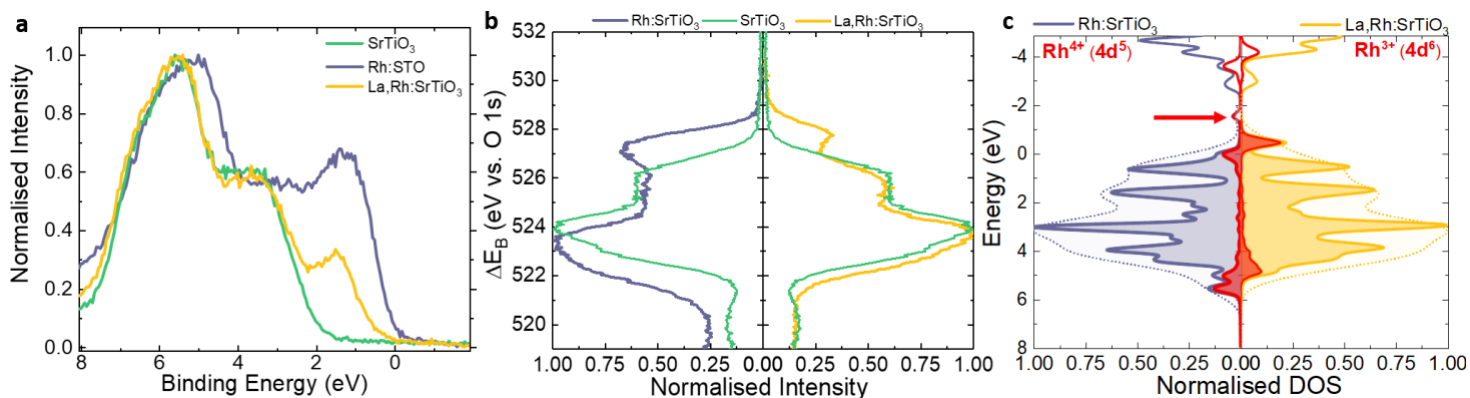
Figure 3. Effect of Rh and La doping on theoretical and experimental band structure of SrTiO₃. (a) Valence XPS spectra of SrTiO₃, Rh:SrTiO₃, and La,Rh:SrTiO₃. The larger area of the peak introduced by Rh doping in Rh:SrTiO₃ is attributed to increased surface segregation of Rh in Rh:SrTiO₃ (Supplementary Fig. S2.1, Table S1).(b) VB spectra of the samples on the ΔE_B scale enable direct comparison of the energy of the Rh dopant states. (c)The density of states calculated by hybrid DFT, aligned using O 2p states and weighted by the elemental single electron ionisation cross-section for the Al Kα X-rays used in our XPS studies. Rh 4d states are shown in red. To approximate further broadening, an additional gaussian broadening was applied to the peaks, leading to the envelope shown by the dotted line. Unlike XPS, DFT also gives the density of unoccupied states. The red arrow points to an unoccupied Rh state in the mid gap of Rh:SrTiO₃ that is absent in La,Rh:SrTiO₃.

To better understand the link between the fundamental photophysical properties of (La),Rh:SrTiO₃ and the oxidation state of Rh, we turn to DFT-supported VB XPS. Comparing VB spectra of SrTiO₃, Rh:SrTiO₃ and La,Rh:SrTiO₃ (Fig. 3a), we observe a significant Fermi level (E_F) shift in both Rh-doped oxides towards the effective VB edge, consistent with p-type conductivity as observed by Kudo et al.[34] E_F of SrTiO₃, Rh:SrTiO₃ and La,Rh:SrTiO₃ is located ~1.8 eV, ~0.1 eV and ~0.3 eV above their respective VB edges (linear extrapolation see Supplementary Fig. S2.1f). As a result, all peaks shift in accordance with the observed Fermi level change seen in the VB spectrum (Supplementary Figure S2.2a), consistent with previous observations of Rh doped oxides.[35,36] This effect prevents direct comparison of relative energies of Rh states in the VB region on the binding energy (E_B) scale.[35] However, the binding energy relative to lattice O²⁻ in the O 1s spectrum (ΔE_B vs O 1s) should be independent of this effect[36] (Supplementary Figure S2.2a and accompanying equation). Comparison of the VB spectra of doped and undoped materials, plotted relative to the lattice O²⁻ binding energy (Fig. 3b), allows us to see that Rh doping introduces states above the VB maximum and below the VB minimum of SrTiO₃, leading to a broadening of the VB envelope and a narrowing of the effective band gap, consistent with our observations in Fig. 1a. Closer inspection of the region around the VB maximum (Supplementary Fig. S2.2b) shows that the states introduced by Rh doping are shifted to higher energy upon La co-doping. The same effect is also observed when Rh:SrTiO₃ is reduced in a hydrogen atmosphere (Supplementary Figure S2.3f), implying that this shift is the result of Rh⁴⁺ reduction rather than any additional orbital contribution from La. This effect is consistent with the red shift in the effective band edge observed when Rh:SrTiO₃ is reduced (Fig. 2a,b).

To verify our analysis of the VB spectra, and to provide insight into the nature of the Rh states introduced by doping, we turned to hybrid DFT. The HSE06 functional was combined with an unprecedentedly large 3x3x3 supercell to enable accurate reproduction of the nominal Rh-doping concentration to calculate and compare the electronic structure of doped, co-doped and undoped SrTiO₃ (see Methods for further details). The calculated densities of states (DOS) for the VB region of Rh:SrTiO₃ and La,Rh:SrTiO₃ (Fig. 3c) reveal that the broadening of the VB region observed experimentally upon Rh doping is caused by the introduction of Rh 4d states
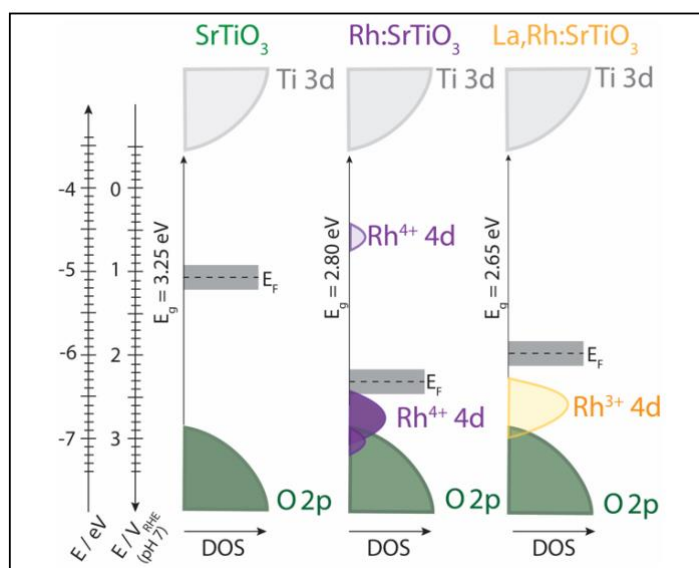
Figure 4. A simplified electronic structure model. Energy band diagrams of $SrTiO_3$, $Rh:SrTiO_3$ and $La:SrTiO_3$ determined from the combined results of our XPS, UV-vis, (spectro)electrochemistry measurements and DFT calculations. Plotted is the density of states (DOS) on the absolute energy scale as well as on the reversible hydrogen electrode (RHE) scale at pH 7. Fermi level positions (E_F) and band gap energies (E_g) and the position of the vacant Rh^{4+} mid gap level in $Rh:SrTiO_3$ are also indicated. See main text for more details.

above the VB maximum and below the VB minimum of $SrTiO_3$. Moreover, DFT accurately predicts that in $Rh:SrTiO_3$, Rh 4d states are more deeply situated than in $La,Rh:SrTiO_3$, which is verified by our experiments as detailed above (Fig. 1a and 3b). No La orbital character is observed near the band edges (Supplementary Fig. S6.1b), consistent with the concept that La^{3+} induces the reduction of Rh^{4+} via an ionic charge compensation mechanism but does not directly alter band edge composition.[29] Most strikingly, a vacant mid gap state with Rh 4d character is observed in $Rh:SrTiO_3$ (red arrow, Fig. 3c) which is absent in $La,Rh:SrTiO_3$. As this state does not have La orbital character, and an analogous effect can be achieved by introducing an electron to $Rh:SrTiO_3$ in the presence of a compensating background charge (which localises on Rh^{4+} during optimisation, Supplementary Fig. S6.1d, S6.2), we attribute this change to Rh^{4+} reduction. Further, integration of the Rh 4d DOS shows that the density of filled Rh 4d states at the VB edge effectively increases by one electron upon reduction. This indicates that the Rh 4d electronic structure re-arranges as an electron is added to Rh^{4+} and the mid gap state is incorporated into the VB (for discussion see Supplementary Fig. S6.2, S6.3). Figure 4 summarises energy band diagrams of $SrTiO_3$ and its doped equivalents determined from our SEC and DFT-supported XPS experiments. From DFT we obtain electron affinities, which are in good agreement with literature values for CB edge energies (E_{CB}) of $SrTiO_3$,[37] and indicate that E_{CB} is largely insensitive to doping (Supplementary Fig. S6.4). As DFT calculations often slightly underestimate E_g, we use our UV-vis spectra (Fig. 1a) to position the VB edge energies on an absolute energy scale, in reasonable agreement with our calculated ionisation potentials (Supplementary Fig. S6.4). From VB XPS (Fig. 3a), we estimate the Fermi level position relative to the VB (in the absence of band bending) and find it to be in excellent agreement with independent measurements of a very positive flatband potential of $La,Rh:SrTiO_3$ photocatalyst sheets ($+1.8$ V_{RHE}) using impedance spectroscopy, consistent with reported p-type character.[24,30,31] Finally, we estimate the reduction potential of Rh^{4+} states using the half-wave potential obtained from SEC (Supplementary Fig. S4b) and combine it with our DFT results to locate the vacant mid-gap state.
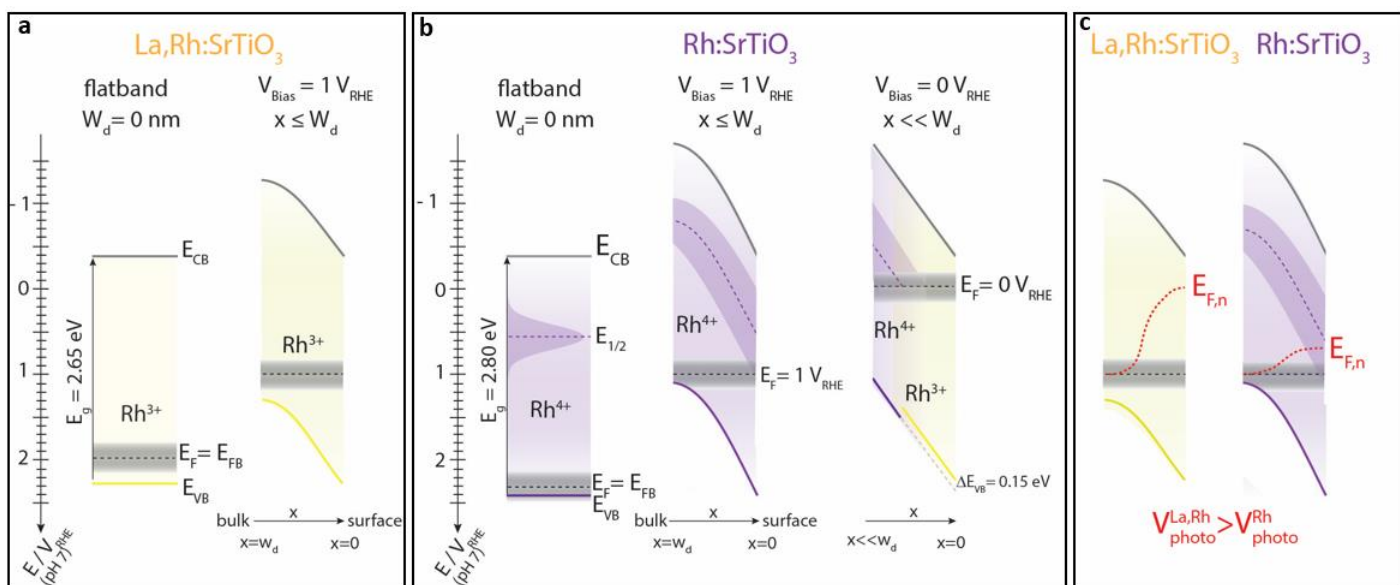
Figure 5. A simple surface depletion model explaining the in-situ charge carrier dynamics of (La,)Rh:SrTiO₃ photocatalyst sheets. Model of surface depletion in La,Rh:SrTiO₃ (a) and Rh:SrTiO₃ (b) at different applied potentials in the dark. The flatband condition ($E_F=E_{FB}$) for both materials is adapted from Fig. 4. At 1 V_{RHE}, there is significant band bending in both La,Rh:SrTiO₃ and Rh:SrTiO₃ (with W_d indicating the space charge layer width). However, in Rh:SrTiO₃, the Fermi level (E_F) does not exceed the reduction potential of the vacant Rh^{4+} level ($E_{1/2}$, purple dashed line), leading to Rh adopting the 4+ oxidation state in the entire material and in the depletion layer ($x<W_d$). At 0 V_{RHE}, the energy of Rh^{4+} at the surface of the depletion region ($d \ll W_d$) falls below the Fermi level and Rh^{4+} becomes reduced, leading to a re-organisation of the Rh 4d states – adopting the electronic configuration of a reduced Rh:SrTiO₃ (indicated by yellow colouring), which is almost identical to that of La,Rh:SrTiO₃. This is corroborated by a 0.15 eV red-shift in the effective band gap that we observe in our SEC experiments (Fig. 2a). (c) Photovoltage build-up in La,Rh:SrTiO₃ and Rh:SrTiO₃ under illumination at positive device operation potentials. Here, conduction band electrons can accumulate in La,Rh:SrTiO₃ due to strong downward band bending leading to effective charge separation. This is indicated by a quasi-Fermi level for electrons ($E_{F,n}$) reaching towards the CB. In Rh:SrTiO₃, a similarly strong potential drop develops at the surface, however, trapping processes likely related to the trapping of electrons by Rh^{4+} states prevent the accumulation of electrons, indicated by a quasi-Fermi level pinned to the Rh^{4+} redox potential. This in turn leads to smaller photovoltage developing in Rh:SrTiO₃.

In Figure 5, we use the energy band diagrams in Figure 4 to illustrate the expected potential-dependence of depletion layer formation in (La),Rh:SrTiO₃, and relate these to our potential-dependent SEC, PIA and TA measurements (Fig. 2). A striking result of this analysis is that in both La,Rh:SrTiO₃ (Fig. 5a) and Rh:SrTiO₃ (Fig. 5b), a strong potential drop at the semiconductor-electrolyte liquid junction is created even at the most positive potentials studied (e.g. 1 V_{RHE}) due to their strongly positive flatband potentials (Fig 4). The field in the depletion region at these potentials appears to be sufficient to efficiently separate charge in La,Rh:SrTiO₃, as inducing a further volt of band bending (i.e. at 0 V_{RHE}) yields only a modest increase in the photogeneration of long-lived CB electrons under operational conditions (Fig. 2e). This implies that the downward shift in flatland potentials induced by Rh doping drives effective charge separation even at positive applied potentials. This is consistent with the remarkably early onset potentials (up to 1.2 V_{RHE}) previously observed in photocatalyst sheet half-electrodes.[25] However, despite a similar flatband potential to La,Rh:SrTiO₃, Rh:SrTiO₃ is unable to photogenerate long-lived electrons at equivalent positive potentials (i.e. 1 V_{RHE}). Instead, Rh:SrTiO₃ shows a yield of CB electrons which tracks the redox wave originating from Rh^{4+} reduction (Fig. 2f, Supplementary Fig. S4b), with the largest changes occurring around $E_{1/2}$ of the Rh^{4+}/Rh^{3+} redox couple. Only at potentials negative of this redox potential do the yields and lifetimes of CB electrons in Rh:SrTiO₃ and La,Rh:SrTiO₃ converge. In Figure 5c we use our model to explain this behaviour. At potentials positive of $E_{1/2}$, minority carriers in Rh:SrTiO₃ are trapped and recombine via mid-gap Rh^{4+} states. The quasi-Fermi level of electrons ($E_{F,n}$) is therefore likely to be pinned to these mid-gap states, leading to a diminished photovoltage in comparison to La,Rh:SrTiO₃ (Supplementary Fig. 7). At potentials
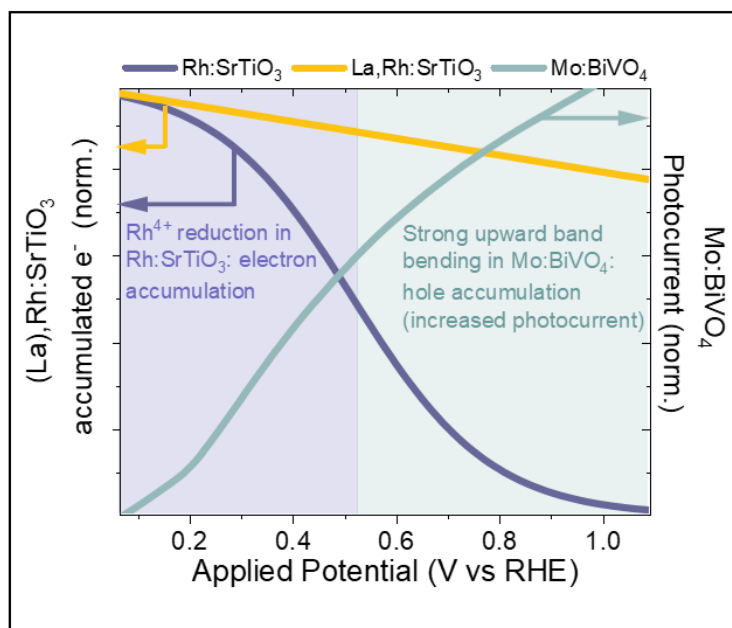
Figure 6. The role of Rh oxidation state and La co-doping in determining the performance of a Mo:BiVO₄/(La),Rh:SrTiO₃ Z-scheme device.
Electron accumulation under operational conditions in (La),Rh:SrTiO₃ (Fig. 2f) plotted alongside a normalised J-V curve for typical Mo:BiVO₄ photocatalyst sheets in the presence of a Fe/Ni based co-catalyst.[17]

negative of $E_{1/2}$, Rh^{4+} states in the depletion layer are reduced, and persistent CB electrons are observed (Fig. 2d). Hence, La co-doping can be understood as obviating the need for the strong negative potentials ($\ll 0.52$ V_{RHE}) or chemically reducing conditions[23,25,27,38] that would be otherwise required to reduce surface Rh^{4+} states. This suppresses electron trapping, leading to the build-up of a higher photovoltage due to the accumulation of minority carriers on timescales of the water splitting reaction.

Due to current matching requirements, the operation of complete photocatalyst sheet devices is thus also Rh oxidation state dependent. Hence, in a Rh:SrTiO₃/Mo:BiVO₄ device, large yields of persistent electrons in Rh:SrTiO₃ can solely be obtained closer to the flatband potential of Mo:BiVO₄ (ca. 0.1 V_{RHE}[39]) or, in other words, close to the onset of photocurrent for an optimal Mo:BiVO₄ photoanode.[40,41] In contrast, in a La,Rh:SrTiO₃/Mo:BiVO₄ device, La fixes the Rh oxidation state to Rh^{3+} and removes the Rh^{4+} mid-gap level *without compromising the position of the Fermi level.* This leads to accumulation of CB electrons even at remarkably positive potentials. This is illustrated in Figure 6 where the population of accumulated CB electrons in (La),Rh:SrTiO₃ sheets (taken from Fig. 2f) is plotted alongside a JV curve of a previously reported typical Mo:BiVO₄ photocatalyst sheet half electrode.[17] Figure 6 predicts that the crossing point of Rh:SrTiO₃/Mo:BiVO₄ device would be at more negative potentials, where the Rh:SrTiO₃ surface is only partially reduced and the predicted photocurrent low. On the other hand, a La,Rh:SrTiO₃/Mo:BiVO₄ crosses at a significantly more positive potential, at which photogeneration of long-lived charge carriers is high in both Mo:BiVO₄ and La,Rh:SrTiO₃, enabling both efficient proton reduction and water oxidation. The more positive crossing point of the respective half-cell J-E curves in turn leads to a Z-scheme photocatalyst sheet device requiring a metal contact with a high work function (i.e. Au), consistent with calculations in the work of Wang *et al.*[26] The carrier dynamics of this interface are of significant interest. However, the surface selective nature of the measurements presented here preclude study of the back contact.

It is remarkable that chemical reduction of Rh:SrTiO₃ does not compromise the position of the Fermi level as would be expected from simply considering the filling of the Rh^{4+} mid gap level upon reduction in the absence of any reorganization. We therefore consider the oxidation state

dependent Rh 4d electronic structure to be a crucial and distinguishing operational parameter in this material, as conservation of the position of the Fermi level upon chemical reduction leads to extremely positive flatband potentials being observed in the Rh-doped and La,Rh co-doped materials alike. This drives strong band bending at the semiconductor/electrolyte interface in-situ, meaning that charge separation is limited by density of the vacant mid gap levels associated only with Rh^{4+} rather than the strength or width of the depletion layer. Thus, co-doping with La reduces Rh^{4+}; removing mid gap levels without strongly influencing band bending. This drives a positive shift in the crossing point of the complete Z-scheme device towards a crossing point where both water oxidation and proton reduction occurs efficiently.

In conclusion, by linking charge accumulation to electronic structure in $(La),Rh:SrTiO_3$ we are able to explain the record device operation of the $La,Rh:SrTiO_3/Mo:BiVO_4$ photocatalyst sheets. We find that Rh doping narrows the effective optical gap of $SrTiO_3$ and induces a strong downward shift in flatband potential, successfully creating a p-type visible light absorber. Using Rh alone to dope the wide band gap absorber produces a vacant mid-gap Rh 4d state. During illumination, this state prevents the accumulation of electrons near the conduction band and instead promotes charge trapping and recombination. Reduction of Rh^{4+} leads to a reorganization of Rh 4d orbitals, integrating this state into the valence band region. While the reduction to Rh^{3+} can be driven by negative applied potential or by a reductive annealing treatment, co-doping with La appears to be an elegant strategy to effectively and persistently mitigate the formation of the mid-gap state without compromising p-type character. In the absence of a mid-gap state, the strongly positive flatband potential of $La,Rh:SrTiO_3$ enables strong downward band bending even under relatively positive potentials (e.g. +1 V_{RHE}), enabling bipolar charge accumulation in the device at potentials where both the n- and p-type semiconductors separate charge efficiently.

More broadly, this work identifies both electronic structure reorganisation and Fermi level effects as key parameters that must be considered in engineering novel functional visible light absorbing materials for photocatalysis. The insights gained herein lead to a deeper understanding of the interplay between electronic structure, dopant oxidation states, minority carrier lifetimes and device operation in cutting edge photocatalyst devices. Having identified the crucial role of co-doping in the function of the complete Z-scheme device, we note that a necessary prerequisite to succeeding in creating new band gap engineered visible light absorbers may be the choice of a perovskite (ABX_3) host lattice, such as $SrTiO_3$, where two cation sites can be substituted independently of one another in a crystal lattice that is structurally tolerant to doping. This represents a crucial break from studies on TiO_2, where only one cation site can be substituted in a lattice that is itself less tolerant to doping.[36]

Author Contributions

Corresponding author

Correspondence to Dr Ludmilla Steier. l.steier@imperial.ac.uk

Competing interests

The authors declare no competing interests.

Data Availability

The data presented in the main body of this paper is available in csv format on Zenodo at http://doi.org/10.5281/zenodo.4063942 and source data is available in opj format also on Zenodo at http://doi.org/10.5281/zenodo.4071556. Both can be used under the Creative Commons Attribution licence 4.0.

Methods

Synthesis of Rh and La,Rh:SrTiO₃: Rh:SrTiO$_3$ and La,Rh:SrTiO$_3$ were synthesised by a previously reported two step solid state reaction.[25,42] In the first step, rutile TiO$_2$ (Kanto Chemicals, 99.0%) and SrCO$_3$ (Kanto Chemicals, 99.9%, calcined in air at 573 K for 1 h) were ground in a mortar to obtain a mixture with a Sr/Ti ratio of 1.05. The mixture was then calcined at 1423 K for 10 h to produce SrTiO$_3$. In the second step, SrTiO$_3$ was ground in ethanol with Rh$_2$O$_3$ (Kanto Chemicals, 99.9%) and calcined at 1373 K for 6 h to make Rh:SrTiO$_3$. For La,Rh:SrTiO$_3$ fabrication, both La$_2$O$_3$ (Kanto Chemicals, 99.99%, freshly calcined in air at 1273 K for 12 h) and Rh$_2$O$_3$ (Kanto Chemicals, 99.9%) were calcined at 1373 K for 6 h. In both cases, La and Rh was added such that the nominal doping concentration (i.e [Rh]/([Rh]+[Ti] or [La]/([La]+[Sr]) was 4 mol%. H$_2$-Rh:SrTiO$_3$ was produced by annealing Rh:SrTiO$_3$ powder at 573 K in a hydrogen atmosphere for two hours. For transient absorption scavenger studies, films were fabricated directly from powders by dispersing 50 mg of powder in water, drop casting on to glass and calcining at 673 K for 1 h.

Fabrication of photocatalyst sheets: (La),Rh:SrTiO$_3$ photocatalyst sheets were fabricated by a modified particle transfer method. The procedure was identical to previous reports except that Mo:BiVO$_4$ particles were omitted and a much thicker Au layer (ca. 2 µm as opposed to ca. 350 nm) was used to create a continuously conductive back contact. Doped SrTiO$_3$ (20 mg) was suspended in isopropanol (99.9%, 0.5 ml), drop-cast on a glass substrate (3×3 cm^2) and left to dry at room temperature overnight. The Au back contact was then deposited by thermal vacuum evaporation (VFR-200M/ERH, ULVAC KIKO) at an evaporation rate of approximately 20 nm s^{-1} at a base pressure of 2.6×10^{-3} Pa. The exposed Au surface was then bonded to a second glass plate (3×3 cm^2) with double sided carbon tape and lifted off the primary glass plate. The resulting photocatalyst sheet was then ultrasonicated twice in distilled water for 2 minutes to remove any unattached particles.

Scanning electron microscopy (SEM): SEM images were taken on a LEO GEMINI 1525 microscope using a 1.5 keV electron beam and a secondary electron detector. As the back Au contact in the

photocatalyst sheets provides a highly conductive pathway for charge, no conductive coating was required. EDX was performed on the same instrument using an Oxford Instruments X-act detector at a beam voltage of 20 keV and a 60 mm aperture.

X-ray photoelectron spectroscopy (XPS): XPS was performed on a Thermo Scientific K-alpha+ instrument. Powdered samples were attached to a stainless-steel plate using conductive carbon tape. The instrument uses monochromated and microfocused Al Kα (hν = 1486.6 eV) radiation to eject photoelectrons which are then analysed using a 180° double-focusing hemispherical analyser with a 2D detector. Spectra were collected at $2x10^{-9}$ mbar base pressure. A flood gun was used to minimize sample charging. All samples were referenced against the C-C peak of adventitious carbon in the C 1s spectrum at a binding energy of 284.8 eV to correct for any charge that is not neutralised by the flood gun. Further effects were then accounted for by taking the separation from the O 1s oxide peak. Data was analysed using the CASA XPS package.

Ultraviolet-visible absorption spectroscopy and spectroelectrochemistry: Reflectance spectra of the photocatalyst sheets were collected using a Shimadzu UV-vis 2600 spectrophotometer equipped with an integrating sphere, using a disk of pressed barium sulphate as a 100% reflecting reference. The resulting diffuse reflectance spectra were then converted to a unit proportional to absorptance using the Kubelka-Munk function, $F(R) = \frac{k}{s} = \frac{(1-R)^2}{(2R)}$. Where k and s respectively correspond to absorption and scattering coefficients and R corresponds to the reflectance (the fraction of light reflected in comparison to the fully scattering $BaSO_4$ reference). For spectroelectrochemical measurements, photocatalyst sheets were measured in a quartz cuvette in three-electrode configuration using an Ag/AgCl (sat'd KCl) reference electrode, a platinum mesh counter electrode and the doped $SrTiO_3$ working electrodes in 0.1 M Na_2SO_4 electrolyte (pH 7). Potentials were applied using a Metrohm Autolab PGSTAT 101 potentiostat. Reflection and refraction from the cuvette do not change with applied potential and so did not contribute to the observed change in the Kubelka-Munk function. A small offset at 820 nm is visible due to a change in detector and a low background level of reflected light in this experiment.

Hybrid Density functional calculations: All calculations are performed using the VASP package.[43] For doping calculations a 3x3x3 supercell was created. In the case of co-doping all symmetry inequivalent positions of the dopants were explored, although no qualitative and very little quantitative differences were found. We therefore use a single configuration for presenting our results. For relaxation of atomic positions the PBEsol functional[44], projector augmented pseudopotentials[45], and a cut-off energy of 500 eV, with k-point sampling defined as an evenly spaced grid in reciprocal space with a density scaled to the unit cell size were used to achieve uniform sampling with a target length cut-off of 10 Å, as described by Moreno and Soler[46] . The relaxed structures were then used for input to hybrid DFT calculations using the HSE06 functional[44] to calculate accurate electronic structure.

Diffuse reflectance transient absorption and photoinduced absorption: Transient absorption and photoinduced absorption measurements were carried out on a home built setup described in our previous publications.[47] Briefly, micro-second to second transient absorption decays were acquired by measuring the diffuse reflectance of the opaque samples studied herein. A Nd:YAG laser (OPOTEK Opolette 355 II, 7 ns pulse width) was used as the excitation source, producing 355 nm light that was transmitted to the sample using a liquid light guide. An excitation power density of 400 µJ/cm^2 was typically used in conjunction with a laser repetition rate of 0.8 Hz. Probe light was generated by a 100 W Bentham IL1 quartz halogen lamp. Long pass filters (Comar Instruments) and an IR filter (H_2O, 5 cm path length) were positioned between the lamp and sample to minimise short wavelength irradiation and heating of the sample. Diffuse reflectance from the sample was collected and relayed to a monochromator (Oriel Cornerstone 130) through a long pass filter to select the probe wavelength. Acquisitions were triggered by a photodiode (Thorlabs DET10A) exposed to laser scatter. A Si photodiode (Hamamatsu S3071) was used as a detector in the visible region and an InGaAs diode (Hamamatsu G10899-03K) in the near IR. Data at times faster than 2 ms were amplified by custom electronics and recorded by an oscilloscope (Tektronics DPO3012) while data slower than 2 ms was simultaneously recorded on a National Instrument DAQ card (NI USB-6251). Kinetic traces were typically obtained from the average of 100

laser pulses. Data was acquired and processed using software written in the LabVIEW environment (Austin Consultants). Photoinduced absorption data, were collected with the same setup replacing the laser pulse by a continuous wave illumination of a 365 nm LED at an intensity of 8 mW cm^{-2}, corresponding to ½ sun of absorbed photons assuming a sharp absorption edge at 470 nm. The percentage change in reflectance was calculated according to pioneering work by Wilkinson and co-workers.[48] Here the fractional change in reflected light due to transient absorption is:

$$R_t = \frac{V_t - V_0}{V_0}$$

Where V_0 is the voltage arising on Si photodiode from the probe beam before the pump, V_t is the voltage on the diode at time t after the pump. The % change in absorption (% *Abs.)* is thus:

$$\% \, Abs = (1 - R_t) \cdot 100$$

The changes of reflectance observed were low, with the largest signals being on the order of 1%. This enabled the transient signal to be taken as directly proportional to the concentration of excited state species. [49]

References

1. Fujishima, A., Zhang, X. & Tryk, D. A. TiO2 photocatalysis and related surface phenomena. *Surface Science Reports* vol. 63 515–582 (2008).
2. Pai, Y. Y., Tylan-Tyler, A., Irvin, P. & Levy, J. Physics of SrTiO3 - based heterostructures and nanostructures: A review. *Reports on Progress in Physics* vol. 81 (2018).
3. Goto, Y. *et al.* A Particulate Photocatalyst Water-Splitting Panel for Large-Scale Solar Hydrogen Generation. *Joule* **2**, 509–520 (2018).
4. Zhao, Z. *et al.* Electronic structure basis for enhanced overall water splitting photocatalysis with aluminum doped SrTiO3 in natural sunlight. *Energy Environ. Sci.* **12**, 1385–1395 (2019).
5. Abe, R. Recent progress on photocatalytic and photoelectrochemical water splitting under visible light irradiation. *J. Photochem. Photobiol. C Photochem. Rev.* **11**, 179–209 (2011).
6. Khan, S. U. M., Al-Shahry, M. & Ingler, W. B. Efficient photochemical water splitting by a chemically modified n-TiO2. *Science (80-.).* **297**, 2243–2245 (2002).
7. Asahi, R., Morikawa, T., Ohwaki, T., Aoki, K. & Taga, Y. Visible-light photocatalysis in nitrogen-doped titanium oxides. *Science (80-.).* **293**, 269–271 (2001).
8. Konta, R., Ishii, T., Kato, H. & Kudo, A. Photocatalytic activities of noble metal ion doped SrTiO3 under visible light irradiation. *J. Phys. Chem. B* **108**, 8992–8995 (2004).
9. Herrmann, J. M., Disdier, J. & Pichat, P. Effect of chromium doping on the electrical and catalytic properties of powder titania under UV and visible illumination. *Chem. Phys. Lett.* **108**, 618–622 (1984).
10. Daghrir, R., Drogui, P. & Robert, D. Modified TiO$_2$ for environmental photocatalytic applications: A review. *Ind. Eng. Chem. Res.* **52**, 3581–3599 (2013).
11. Sakatani, Y. *et al.* Metal ion and N co-doped TiO2 as a visible-light photocatalyst. *J. Mater. Res.* **19**, 2100–2108 (2004).
12. Kudo, A., Niishiro, R., Iwase, A. & Kato, H. Effects of doping of metal cations on morphology, activity, and visible light response of photocatalysts. *Chem. Phys.* **339**, 104–110 (2007).

13. Torres, G. R., Lindgren, T., Lu, J., Granqvist, C. G. & Lindquist, S. E. Photoelectrochemical study of nitrogen-doped titanium dioxide for water oxidation. *J. Phys. Chem. B* **108**, 5995–6003 (2004).

14. Sivula, K. & Van De Krol, R. Semiconducting materials for photoelectrochemical energy conversion. *Nat. Rev. Mater.* **1**, 15010 (2016).

15. Tilley, S. D., Cornuz, M., Sivula, K. & Grätzel, M. Light-inducedwater splitting with hematite: Improved nanostructure and iridium oxide catalysis. *Angew. Chemie - Int. Ed.* **49**, 6405–6408 (2010).

16. Zhong, D. K. & Gamelin, D. R. Photo-electrochemical water oxidation by cobalt catalyst ('Co-Pi')/α-Fe$_2$O$_3$ composite photoanodes: Oxygen evolution and resolution of a kinetic bottleneck. *J. Am. Chem. Soc.* **132**, 4202–4207 (2010).

17. Kuang, Y. *et al.* Ultrastable low-bias water splitting photoanodes via photocorrosion inhibition and in situ catalyst regeneration. *Nat. Energy* **2**, 16191 (2017).

18. Kim, J. H. *et al.* Awakening Solar Water-Splitting Activity of ZnFe2O4 Nanorods by Hybrid Microwave Annealing. *Adv. Energy Mater.* **5**, 1401933 (2015).

19. Li, Y. *et al.* Cobalt phosphate-modified barium-doped tantalum nitride nanorod photoanode with 1.5% solar energy conversion efficiency. *Nat. Commun.* **4**, 2566 (2013).

20. Minegishi, T., Nishimura, N., Kubota, J. & Domen, K. Photoelectrochemical properties of LaTiO$_2$N electrodes prepared by particle transfer for sunlight-driven water splitting. *Chem. Sci.* **4**, 1120–1124 (2013).

21. Maeda, K. *et al.* Photocatalyst releasing hydrogen from water. *Nature* **440**, 295 (2006).

22. Luo, J. *et al.* Cu$_2$O Nanowire Photocathodes for Efficient and Durable Solar Water Splitting. *Nano Lett.* **16**, 1848–1857 (2016).

23. Wang, Q., Hisatomi, T., Ma, S. S. K., Li, Y. & Domen, K. Core/shell structured La- and Rh-Codoped SrTiO3 as a hydrogen evolution photocatalyst in Z-scheme overall water splitting under visible light irradiation. *Chem. Mater.* **26**, 4144–4150 (2014).

24. Wang, Q. *et al.* Z-scheme water splitting using particulate semiconductors immobilized onto metal layers for efficient electron relay. *J. Catal.* **328**, 308–315 (2015).

25. Wang, Q. *et al.* Scalable water splitting on particulate photocatalyst sheets with a solar-to-hydrogen energy conversion efficiency exceeding 1%. *Nat. Mater.* **15**, 611–615 (2016).

26. Wang, Q. *et al.* Particulate photocatalyst sheets based on carbon conductor layer for efficient Z-scheme pure-water splitting at ambient pressure. *J. Am. Chem. Soc.* **139**, 1675–1683 (2017).

27. Kawasaki, S. *et al.* Elucidation of Rh-induced In-gap states of Rh:SrTiO$_3$ visible-light-driven photocatalyst by soft X-ray spectroscopy and first-principles calculations. *J. Phys. Chem. C* **116**, 24445–24448 (2012).

28. Abe, Y., Kato, K., Kawamura, M. & Sasaki, K. Rhodium and Rhodium Oxide Thin Films Characterized by XPS. *Surf. Sci. Spectra* **8**, 117–125 (2001).

29. Modak, B. & Ghosh, S. K. Exploring the Role of La Codoping beyond Charge Compensation for Enhanced Hydrogen Evolution by Rh-SrTiO3. *J. Phys. Chem. B* **119**, 11089–11098 (2015).

30. Murthy, D. H. K. *et al.* Revealing the role of the Rh valence state, la doping level and Ru cocatalyst in determining the H$_2$ evolution efficiency in doped SrTiO$_3$ photocatalysts. *Sustain. Energy Fuels* **3**, 208–218 (2019).

31. Iwashina, K. & Kudo, A. Rh-doped SrTiO$_3$ photocatalyst electrode showing cathodic photocurrent for water splitting under visible-light irradiation. *J. Am. Chem. Soc.* **133**, 13272–13275 (2011).

32. Godin, R., Kafizas, A. & Durrant, J. R. Electron transfer dynamics in fuel producing photosystems. *Current Opinion in Electrochemistry* vol. 2 136–143 (2017).

33. Murthy, D. H. K. *et al.* Revealing the role of the Rh valence state, la doping level and Ru cocatalyst in determining the H 2 evolution efficiency in doped SrTiO 3 photocatalysts. *Sustain. Energy Fuels* **3**, 208–218 (2019).

34. Iwashina, K. & Kudo, A. Rh-doped SrTiO3 photocatalyst electrode showing cathodic photocurrent for water splitting under visible-light irradiation. *J. Am. Chem. Soc.* **133**, 13272–13275 (2011).

35. Oropeza, F. E. & Egdell, R. G. Control of valence states in Rh-doped TiO2 by Sb co-doping: A study by high resolution X-ray photoemission spectroscopy. *Chem. Phys. Lett.* **515**, 249–253 (2011).

36. Glover, E. N. K., Ellington, S. G., Sankar, G. & Palgrave, R. G. The nature and effects of rhodium and antimony dopants on the electronic structure of TiO2: Towards design of Z-scheme photocatalysts. *J. Mater. Chem. A* **4**, 6946–6954 (2016).

37. Fujisawa, J. ichi, Eda, T. & Hanaya, M. Comparative study of conduction-band and valence-band edges of TiO_2 , $SrTiO_3$, and $BaTiO_2$ by ionization potential measurements. *Chem. Phys. Lett.* **685**, 23–26 (2017).

38. Kawasaki, S. *et al.* Epitaxial Rh-doped SrTiO3 thin film photocathode for water splitting under visible light irradiation. *Appl. Phys. Lett.* **101**, 033910 (2012).

39. Rettie, A. J. E. *et al.* Combined charge carrier transport and photoelectrochemical characterization of BiVO4 single crystals: Intrinsic behavior of a complex metal oxide. *J. Am. Chem. Soc.* **135**, 11389–11396 (2013).

40. Ma, Y., Le Formal, F., Kafizas, A., Pendlebury, S. R. & Durrant, J. R. Efficient suppression of back electron/hole recombination in cobalt phosphate surface-modified undoped bismuth vanadate photoanodes. *J. Mater. Chem. A* **3**, 20649–20657 (2015).

41. Zachäus, C., Abdi, F. F., Peter, L. M. & Van De Krol, R. Photocurrent of BiVO4 is limited by surface recombination, not surface catalysis. *Chem. Sci.* **8**, 3712–3719 (2017).

42. Wang, Q. *et al.* Particulate photocatalyst sheets based on carbon conductor layer for efficient Z-scheme pure-water splitting at ambient pressure. *J. Am. Chem. Soc.* **139**, 1675–1683 (2017).

43. Joubert, D. *From ultrasoft pseudopotentials to the projector augmented-wave method. Physical Review B - Condensed Matter and Materials Physics* vol. 59 (1999).

44. Perdew, J. P. *et al.* Generalized gradient approximation for solids and their surfaces. (2007) doi:10.1103/PhysRevLett.100.136406.

45. Kresse, G. & Furthmüller, J. Efficient iterative schemes for ab initio total-energy calculations using a plane-wave basis set. *Phys. Rev. B - Condens. Matter Mater. Phys.* **54**, 11169–11186 (1996).

46. Moreno, J. & Soler, J. M. Optimal meshes for integrals in real- and reciprocal-space unit cells. *Phys. Rev. B* **45**, 13891–13898 (1992).

47. Godin, R., Wang, Y., Zwijnenburg, M. A., Tang, J. & Durrant, J. R. Time-Resolved Spectroscopic Investigation of Charge Trapping in Carbon Nitrides Photocatalysts for Hydrogen Generation. *J. Am. Chem. Soc.* **139**, 5216–5224 (2017).

48. Wilkinson, F. Diffuse reflectance laser flash photolysis. *J. Photochem.* **17**, 52 (1981).

49. Kessler, R. W., Oelkrug, D. & Wilkinson, F. *The Detection of Transient Spectra within Polycrystalline Samples Using the New Technique of Diffuse Reflectance Flash Photolysis*.